Supplementary Information for: Conformational and state-specific effects in reactions of 2,3-dibromobutadiene with Coulomb-crystallized calcium ions

Ardita Kilaj[1,a], Silvan Käser[1,†], Jia Wang[2,b,†], Patrik Straňák[1,c,†], Max Schwilk[1], Lei Xu[1], O. Anatole von Lilienfeld[1,3,4,5,6], Jochen Küpper[2,7,8,9,**], Markus Meuwly[1,10,**] and Stefan Willitsch[1,**]

[1] Department of Chemistry, University of Basel, Klingelbergstrasse 80, 4056 Basel, Switzerland
[2] Center for Free-Electron Laser Science CFEL, Deutsches Elektronen-Synchrotron DESY, Notkestr. 85, 22607 Hamburg, Germany
[3] Vector Institute for Artificial Intelligence, Toronto, ON, M5S 1M1, Canada
[4] Departments of Chemistry, Materials Science and Engineering, and Physics, University of Toronto, St. George Campus, Toronto, ON M5S 3H6, Canada
[5] Machine Learning Group, Technische Universität Berlin, 10587 Berlin, Germany
[6] Berlin Institute for the Foundations of Learning and Data – BIFOLD, Germany
[7] Department of Physics, Universität Hamburg, Luruper Chaussee 149, 22761 Hamburg, Germany
[8] Department of Chemistry, Universität Hamburg, Martin-Luther-King-Platz 6, 20146 Hamburg, Germany
[9] Center for Ultrafast Imaging, Universität Hamburg, Luruper Chaussee 149, 22761 Hamburg, Germany
[10] Department of Chemistry, Brown University, Providence, RI 02912, USA
[a] Present address: Novartis Institutes for Biomedical Research, Fabrikstrasse 2, 4056 Basel, Switzerland
[b] Present address: Department of Chemistry, University of Hawaii at Manoa, Honolulu, HI 96822, USA
[c] Present address: Fraunhofer Institute for Applied Solid State Physics IAF, Tullastrasse 72, 79108 Freiburg, Germany
† These authors contributed equally to the present work.
** Electronic mail: jochen.kuepper@cfel.de, m.meuwly@unibas.ch, stefan.willitsch@unibas.ch

S1 Simulation of mass spectra

In order to assign masses to the different features observed in the product mass spectrum of Fig. 2a of the main text, simulations of the ion dynamics in the TOF-MS were performed. In mixed-species Coulomb crystals, the ions arrange in layers such that lightest ions are trapped at the center and successively heavier ions accumulate around the lighter ions in shells of increasing radius. This inhomogeneous ion distribution leads to a broadening and bimodal structure of the peaks in the TOF-MS [1].

In the simulations, ion trajectories of a Coulomb crystal being ejected into the TOF-MS were calculated using SIMION [2]. The arrival times at the detector were extracted to determine the mass spectra. In the simulations, a typical Coulomb crystal of 500 Ca^+ ions (mass 40 u) was assumed, additionally containing 20 ions of each of the masses 50 u, 51 u, 52 u, 57 u, 72 u, 120 u and 200 u. A comparison of the experimental data with the simulation is shown in Fig. S1. Different colours highlight the contribution of each ion mass in the simulation. The time coordinates of the simulation have been shifted globally to match the location of the Ca^+ peaks. The locations and splittings of the individual mass peaks reproduce the measured TOF spectra fairly well. A signal due to $CaBr_2^+$ (200 u) is absent in the data. Slight differences between the simulated and observed splittings of the peaks can be explained by different sizes of the simulated and experimental Coulomb crystals.

Based on the good agreement between data and simulation, the product peaks of Fig. S1 were assigned to different molecular compounds as summarized in Table S1.

Table S1: Assignment of molecular compounds to the TOF spectra based on the MD simulation

Mass (u)	Possible compounds
$50, 51, 52$	$C_4H_n^+$, $n = 2, 3, 4$
57	$CaOH^+$
72	CaO_2^+
120	$CaBr^+$
200	$CaBr_2^+$

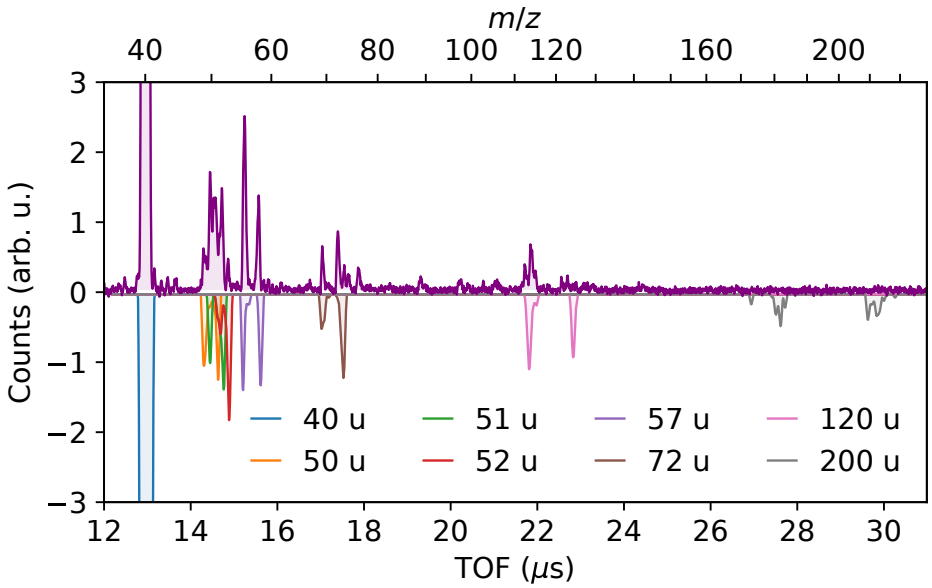

Fig. S1: Comparison of experimental and simulated TOF-MS spectrum. The upper curve shows the measured spectrum while the inverted curve shows a simulated spectrum for 500 ions with mass 40 u and 20 ions of each of the masses 50, 51, 52, 57, 72, 120 and 200 u, highlighted in different colours.

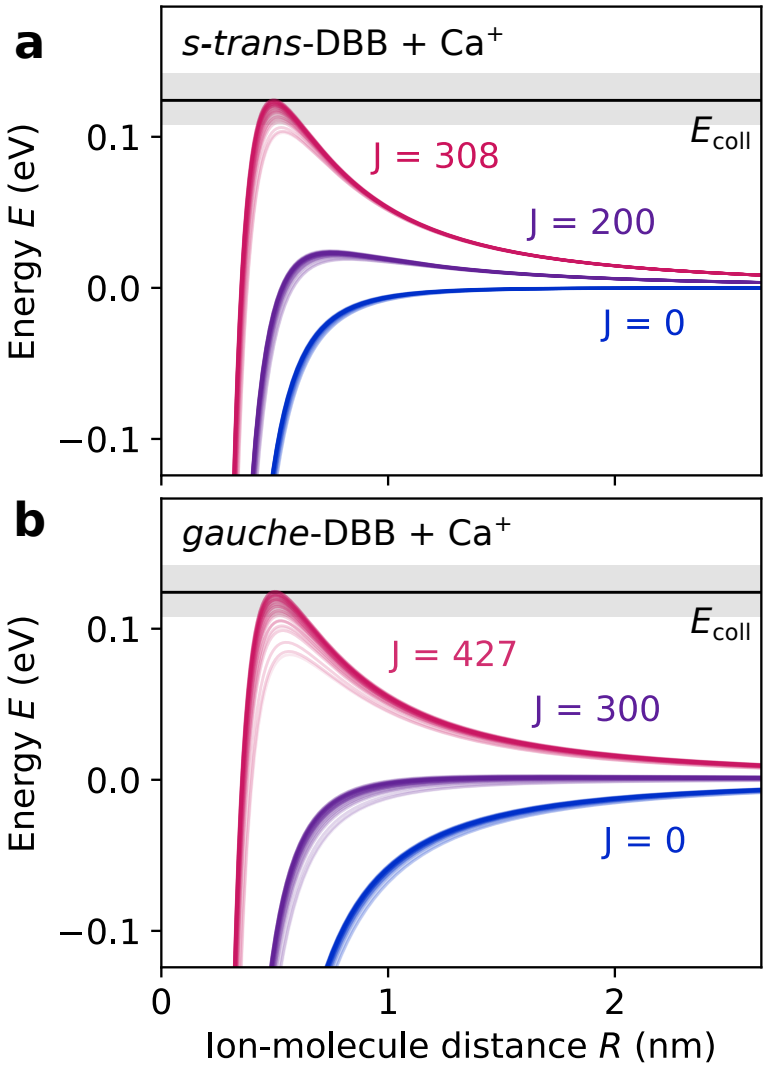

Fig. S2: Long-range ion-molecule interaction potentials. Rotationally-adiabatic and centrifugally-corrected long-range interaction potentials for collisions of *s-trans*- (**a**) and *gauche*-DBB (**b**) with Ca^+. Each value of the total collisional angular momentum J comprises a set of curves corresponding to all rotational states of DBB with rotational angular momentum quantum number $j = 4$, which had the highest population in the experiments. The collision energy E_{coll} is indicated by the black horizontal line and the grey-shaded areas represents its experimental uncertainty.

S2 Adiabatic capture theory

Rotationally adiabatic capture (AC) rate coefficients were calculated using the theory developed by Clary and co-workers [3, 4] that has also been employed in refs. [5, 6]. The AC calculation proceeded in two steps. First, rotationally-adiabatic and centrifugally-corrected long-range interaction potentials were calculated for each rotational state of DBB. The ion-molecule interaction includes charge-induced dipole and charge-permanent dipole couplings. Figs. S2a and b show these long-range potentials for collisions of Ca^+ with *gauche*- and *s-trans*-DBB, respectively. Each set of curves corresponds to a different value of the total collisional angular momentum quantum number J. With increasing J, a centrifugal energy barrier emerges. The individual curves for each value of J belong to all rotational quantum state $|j, \tau, \Omega\rangle$ of DBB with angular momentum quantum number $j = 4$, which is calculated to have the strongest population at $T = 1$ K. The quantum numbers τ and Ω refer to the asymmetric rotor quantum number and the quantum number of the angular-momentum projection onto the ion-molecule distance vector, respectively. Given these long-range potentials, AC theory assigns unit reaction probability to any collision with $J < J_{\mathrm{max}}$, for which the centrifugal energy barrier lies below the experimental collision energy $E_{\mathrm{coll}} = 124(17)$ meV (black solid line in Figs. S2a,b). For each

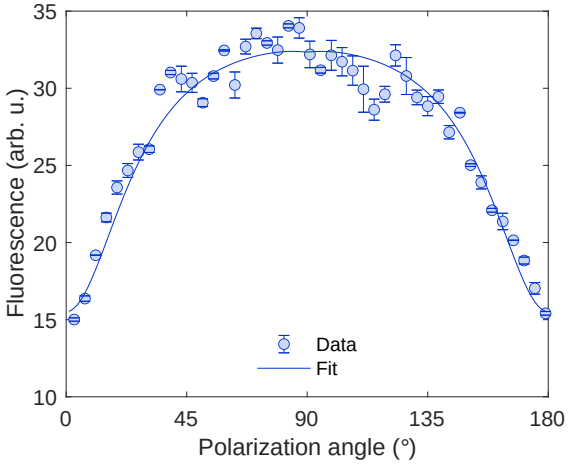

Fig. S3: Polarization scan of the repumper. Ca^+ fluorescence measurement as a function of the 866 nm laser beam polarization angle (data points) and simulated curve from the OBE model. Error bars correspond to one standard deviation.

rotational state $|j, \tau, \Omega\rangle$ of *gauche/s-trans* DBB (g/t), the corresponding value of $J_{\mathrm{max,g/t}}(j, \tau, \Omega, E_{\mathrm{coll}})$ was determined numerically leading to a collisional cross-section [4]

$$\sigma_{\mathrm{g/t}}(j, \tau, \Omega, E_{\mathrm{coll}}) = \frac{\pi\hbar^2}{2\mu E_{\mathrm{coll}}} \left[J_{\mathrm{max,g/t}}(j, \tau, \Omega, E_{\mathrm{coll}}) + 1\right]^2 \tag{S1}$$

where μ is the reduced mass of the two collision partners. The rate coefficient was then calculated by averaging over all rotational states of DBB assuming a thermal distribution, i.e.

$$k_{\mathrm{g/t}}(E_{\mathrm{coll}}, T) = \sqrt{\frac{2E_{\mathrm{coll}}}{\mu}} \sum_{j,\tau,\Omega} p_{\mathrm{g/t}}(T, j, \tau, \Omega)\ \sigma_{\mathrm{g/t}}(j, \tau, \Omega, E_{\mathrm{coll}}) \tag{S2}$$

Here, $p_{\mathrm{g/t}}(T, j, \tau, \Omega)$ is the thermal population of a given rotational state at the rotational temperature T.

Figs. S2a,b show that the centrifugal barrier increases faster with J for *s-trans*-DBB than for *gauche*-DBB such that the maximum collisional angular momenta for a reactive encounter at the experimental collision energy are $J_{\mathrm{max,t}} \approx 308$ and $J_{\mathrm{max,g}} \approx 427$, respectively, implying a larger cross-section $\propto J_{\mathrm{max}}^2$ for *gauche*-DBB. For the lowest values of J, one notices a steeper slope of the ion-molecule potential for *gauche*-DBB. This points to a stronger attractive interaction between the ion and the permanent dipole of *gauche*-DBB as opposed to the apolar *s-trans* conformer and explains the calculated difference in conformer-specific reaction rates. The anisotropic charge-permanent dipole interaction of *gauche* DBB, which is absent for *s-trans* DBB, also leads to a stronger dependence of its rotationally adiabatic potential on the rotational state. This appears as a larger spread between the different potential energy curves for a given value of J.

S3 Determination of Ca^+ electronic state populations

The polarization of the 866 nm repumping laser was adjusted to optimize the repumping efficiency. First, the polarization was cleaned with a polarizing beam-splitter and then rotated using a half-wave plate. Then, the 866 nm beam was combined with the 397 nm light on a dichroic mirror and directed at the ion trap. The polarization of the 397 nm laser was not controlled, since the OBE simulation was found to be insensitive to it. The Ca^+ fluorescence was then measured while varying the polarization angle of the 866 nm repumping laser (Fig. S3). The fluorescence data were fitted using the OBE prediction for the P-state population. At a 90° polarization angle relative to the magnetic field axis

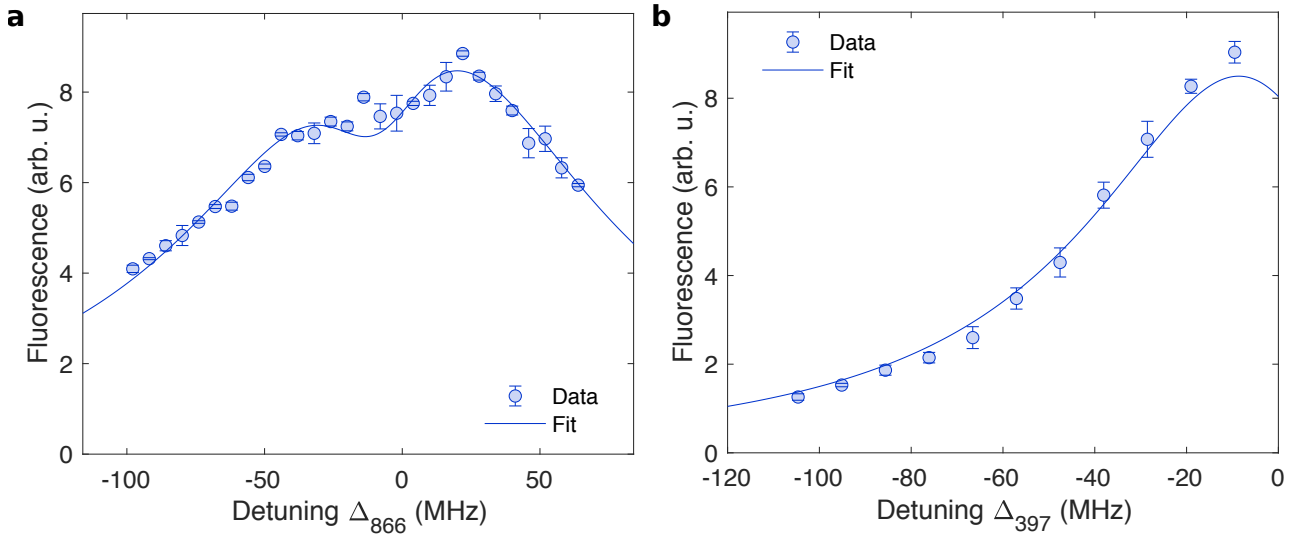

Fig. S4: Fluorescence dependence on laser detunings. Ca^+ fluorescence measurement (data points) as a function of the 866 nm repumping laser detuning (**a**) and the 397 nm cooling laser detuning (**b**). The solid lines are fits to the data based on the OBE model. Error bars correspond to one standard deviation.

the peak fluorescence was found. To maximize population in the $^2P_{1/2}$ state, this setting was used for all subsequent measurements.

After adjusting the polarization, the frequency of the 397 nm cooling laser was set to a detuning of $\Delta_{397} = -10$ MHz, below the "melting point" of the Coulomb crystal at $\Delta_{397} \approx 0$. Then, the Ca^+ fluorescence was measured as a function of the 866 nm repumper detuning Δ_{866} (Fig. S4a). Afterwards, the repumper detuning was set to $\Delta_{866} = 20$ MHz, where repumping is most efficient (Fig. S4a) and the detuning Δ_{397} of the cooling laser was scanned (Fig. S4b). These two datasets were simultaneously fitted using the OBE model, allowing the determination of the following parameters: the effective laser intensities and linewidths, a detuning offset of the 866 nm laser, and a proportionality constant allowing to convert the measured fluorescence to the P-state population. The fitted laser linewidths were consistent with the observed fluctuations on the wavemeter. To optimize the fit, a magnetic field value of 1 Gauss was chosen, which is a reasonable value for the stray magnetic field in the present

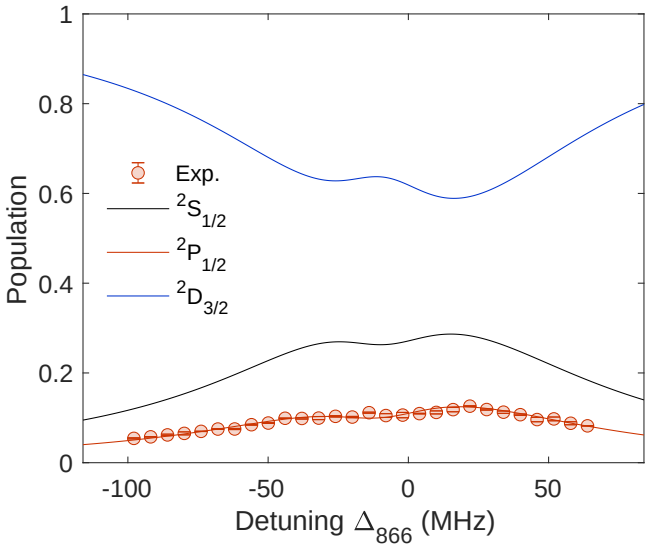

Fig. S5: Ca^+ state population dependence on the repumper detuning. State populations calculated using the OBE with fit parameters from Fig. S4a as function of the 866 nm repumping laser detuning.

apparatus. The resulting $^2S_{1/2}$, $^2P_{1/2}$ and $^2D_{3/2}$ state populations determined from this measurement are shown in Fig. S5. On resonance of the 866 nm repumper, the $^2D_{3/2}$ state population is minimal and the $^2S_{1/2}$, $^2P_{1/2}$ population reach a maximum. The state populations as a function of Δ_{397} resulting from this calibration are shown in Fig. 4a of the main text.

S4 Ground-state potential energy surface of the reaction of DBB with Ca^+

To elucidate the mechanism of the present reaction, the PES of the system was explored using spin-unrestricted density-functional theory (DFT) with both the MPW1K [7] and B3LYP [8, 9] functionals. The def2-TZVPP basis set [10] was employed in both cases. Intrinsic reaction coordinates (IRCs) have been computed independently for both DFT methods. Relevant stationary points on the PES calculated with both methods are shown in Fig. S6. Both functionals yielded qualitatively similar result. Most of the geometries have been located with both methods, except structures **TS1c** and **TS4b** which were found exclusively by MPW1K. The optimized geometries are very similar for both approaches apart from structures **TS3b** and **I5** that differ in bond order. The computed IRCs were found to be the same except for the pathway of **TS2b** connecting to **I4** for MPW1K and to **I5** for B3LYP.

The geometries of the energetically lowest reaction channels found, shown in the main text in Fig. 5, were further reoptimized using the Stuttgart effective core potential (ECP) [11] for the 10 inner shell electrons of bromine atoms for both B3LYP and MPW1K functionals. All structures were confirmed. The geometries were almost identical to the calculations omitting the core potentials. The energy differences and spin contamination were compared in order to investigate the reliability of the structure geometries in Tables S2 and S3 for MPW1K and B3LYP, respectively. Both methods gave very similar relative energies. Restricted open-shell single-point energy calculations were performed

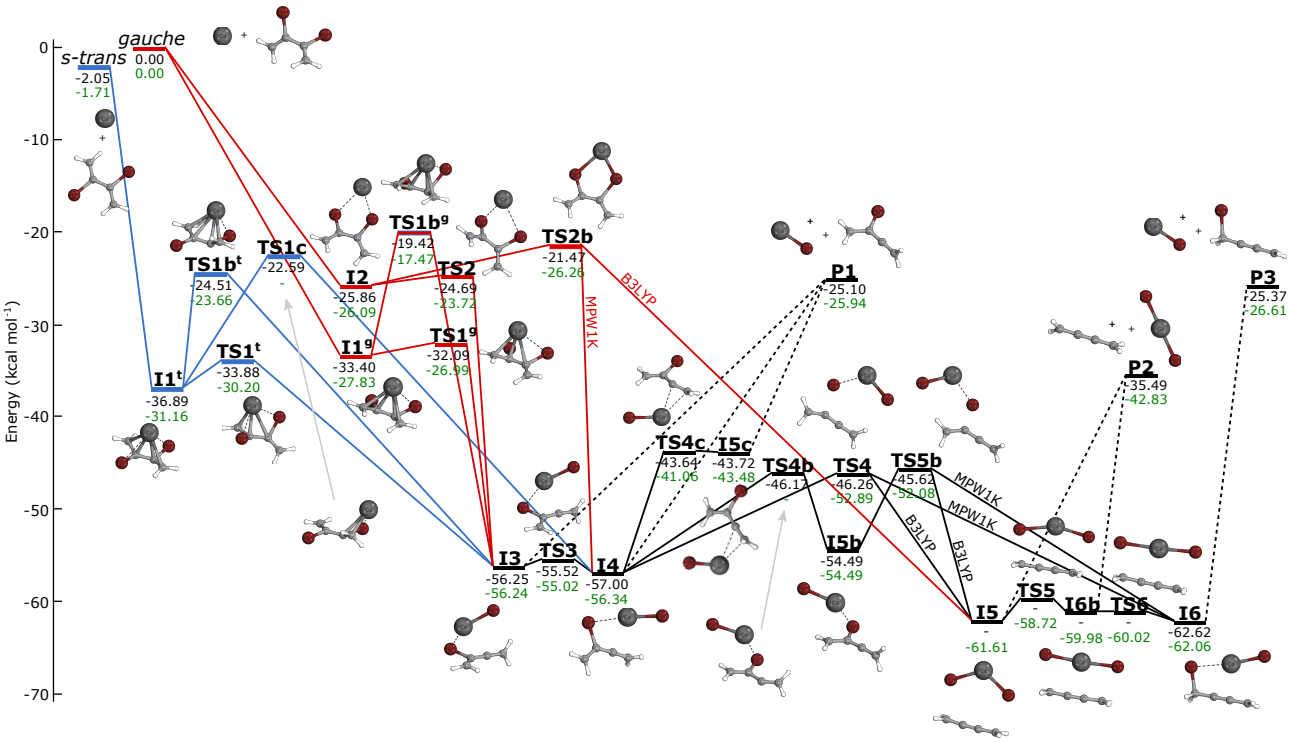

Fig. S6: Extended ground-state potential-energy surface of the reaction of DBB with Ca^+. MPW1K/def2-TZVPP energies are indicated in black, B3LYP/def2-TZVPP energies in green. The energies were corrected for zero-point vibrational motion. IRCs specific to the *s-trans* conformer are shown in blue, for the *gauche* conformer in red. IRCs common to both conformers are depicted in black. The geometries shown were computed with the MPW1K functional.

Table S2: Comparison of single-point energies and squared-spin-operator expectation values $\langle S^2 \rangle$ for MPW1K/def2-TZVPP+ECP.

Name	MPW1K/ def2-TZVPP	MPW1K/ def2-TZVPP+ECP	$\langle S^2 \rangle$
gauche	0.00	0.00	-
s-trans	-2.19	-2.04	-
$I1^g$	-33.12	-30.84	0.7652
$I1^t$	-36.77	-34.31	0.7697
I2	-26.15	-22.50	0.7503
I3	-54.12	-50.32	0.7920
I4	-54.46	-49.55	0.8121
I6	-60.89	-57.02	0.7854
$TS1^g$	-31.39	-27.51	0.7789
$TS1^t$	-32.82	-28.88	0.7699
TS2	-24.95	-21.41	0.7504
TS3	-53.06	-48.45	0.8053
TS4	-42.82	-39.46	0.7988
P1	-22.13	-17.70	0.8113
P2	-31.38	-28.00	0.7928
P3	-22.89	-18.95	0.7946

using Orca [12] on these geometries for further analysis. The single-point energies of the unrestricted and restricted-open-shell B3LYP are very similar suggesting no significant mixing of different electronic states.

Table S3: Comparison of single-point energies for spin-unrestricted B3LYP and spin-restricted open-shell B3LYP (ROB3LYP) as well as squared-spin-operator expectation values $\langle S^2 \rangle$ for B3LYP/def2-TZVPP+ECP.

Name	B3LYP/ def2-TZVPP	B3LYP/ def2-TZVPP+ECP	$\langle S^2 \rangle$	ROB3LYP/ def2-TZVPP+ECP
gauche	0.00	0.00	-	0.00
s-trans	-1.85	-1.79	-	-1.77
$I1^g$	-27.58	-25.43	0.7551	-24.64
$I1^t$	-31.05	-28.92	0.7566	-28.05
I2	-26.19	-23.23	0.7503	-23.14
I3	-54.26	-51.56	0.7685	-49.68
I4	-54.01	-50.50	0.7776	-48.08
I5	-59.51	58.27	0.7643	-57.16
I6	-60.58	-58.16	0.7670	56.37
$TS1^g$	-26.40	-23.36	0.7588	-22.40
$TS1^t$	-29.35	-26.41	0.7622	-25.29
TS2	-23.87	-20.88	0.7503	-20.74
TS3	-52.73	-49.48	0.7746	-47.22
TS4	-49.92	-46.49	0.7739	-44.31
TS5	-56.78	-54.52	0.7624	-53.51
P1	-23.20	-20.22	0.7769	-17.83
P2	-39.20	-37.59	0.7649	-36.36
P3	-24.39	-21.98	0.7713	-19.92

Table S4: Comparison of selected orbitals of intermediate (I) stationary points on the PES computed with spin-restricted B3LYP/def2-TZVPP+ECP and HF/VDZ-F12.

	B3LYP			**HF**		
Structure	SOMO	Ca-Br	π-system	SOMO	Ca-Br	π-system
$I1^g$	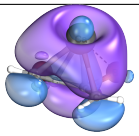	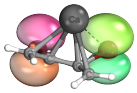	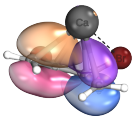	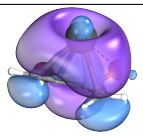	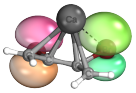	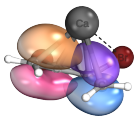
$I1^t$	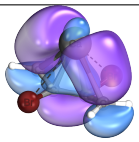	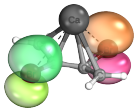	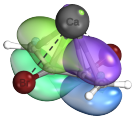	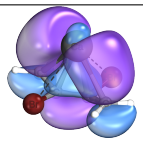	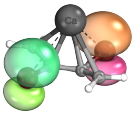	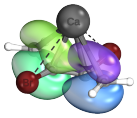
I2	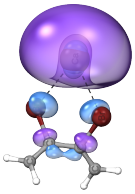	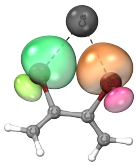	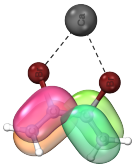	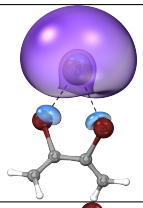	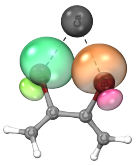	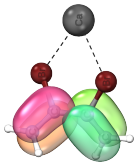
I3	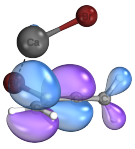	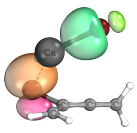	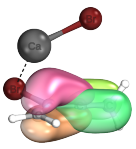	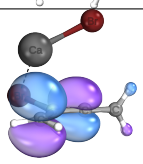	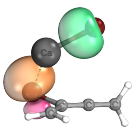	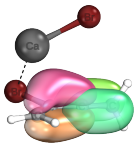
I4	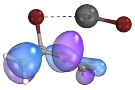	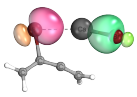	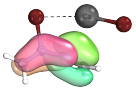	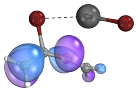	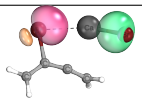	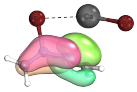
I5	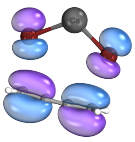	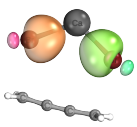	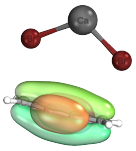	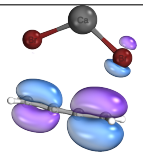	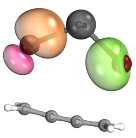	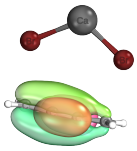
I6	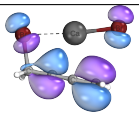		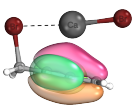	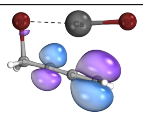		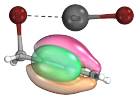

Table S5: Comparison of selected orbitals of transition state (TS) stationary points on the PES computed with spin-restricted B3LYP/def2-TZVPP+ECP and HF/VDZ-F12.

	B3LYP			**HF**		
Structure	SOMO	Ca-Br	π-system	SOMO	Ca-Br	π-system
TS1^g						
TS1^t						
TS2						
TS3						
TS4						

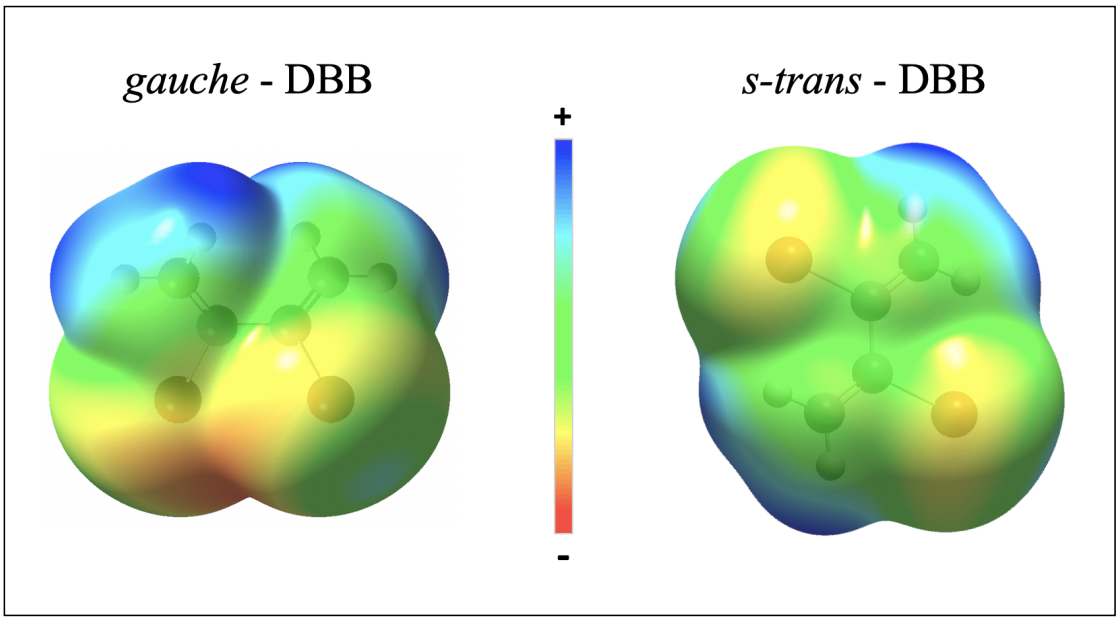

Fig. S7: Molecular charge distributions. Molecular electrostatic potential showing differences in charge distributions of the conformers calculated at B3LYP/def2-TZVPP+ECP level of theory using the Gaussian09 software package.

S5 PhysNet potential energy surface

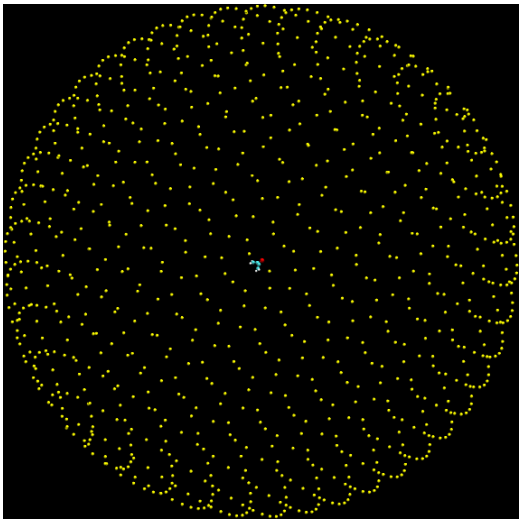

Fig. S8: Fibonacci lattice mapped onto the surface of a sphere generating a homogeneous point distribution on the unit sphere.

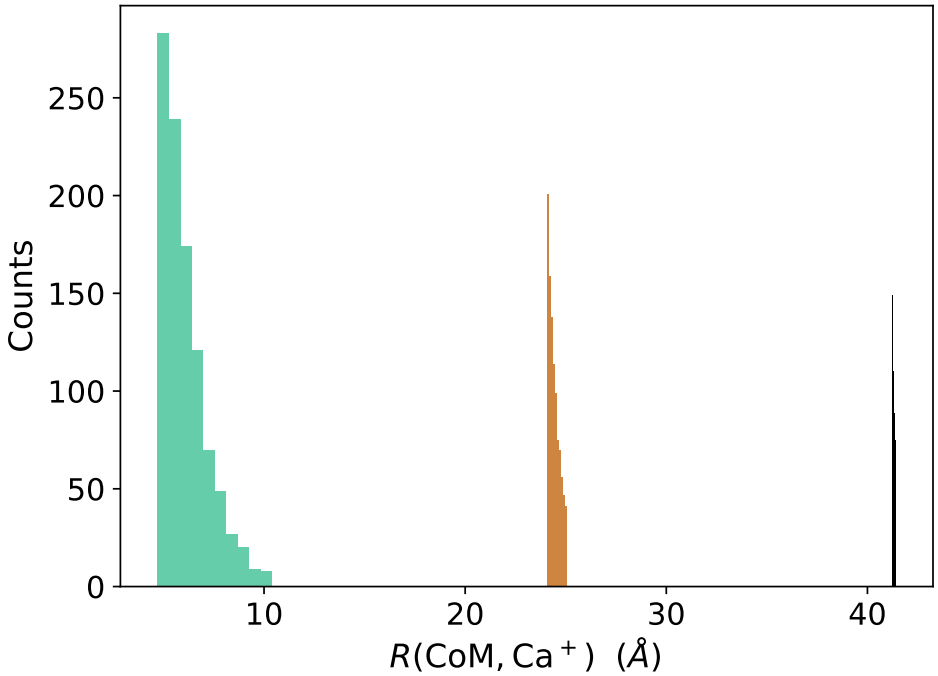

Fig. S9: Histogram of the DBB_{CoM} - Ca^+ distances for all trajectories run for *gauche*-DBB at fixed time intervals. Compare to Fig. 7 of the main text.

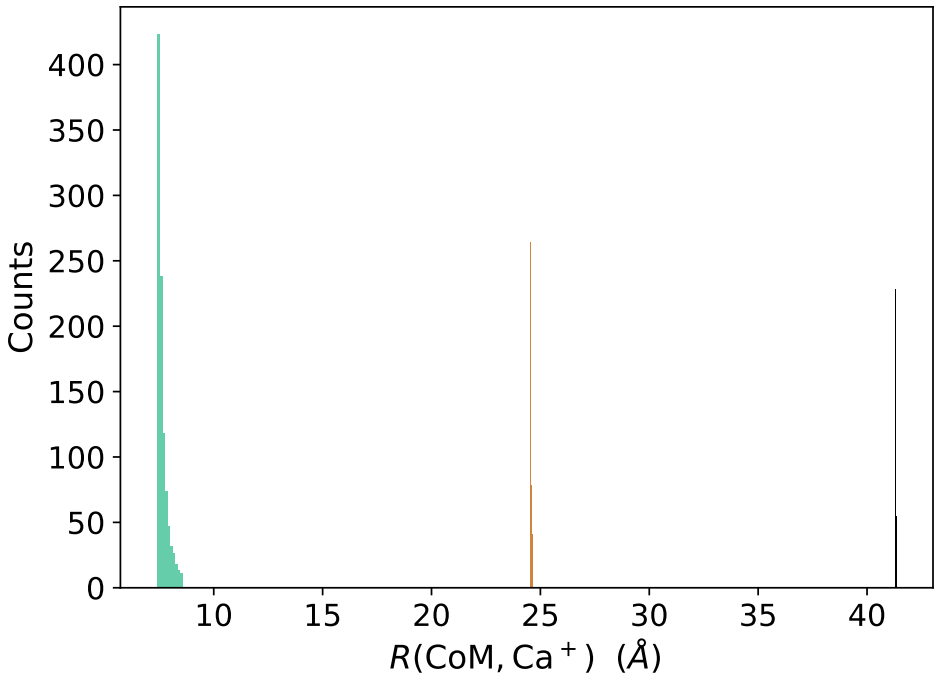

Fig. S10: Histogram of the $\mathrm{DBB}_{\mathrm{CoM}}$ - Ca^+ distances for all trajectories run for *s-trans*-DBB at fixed time intervals. Compare to Fig. 8 of the main text.

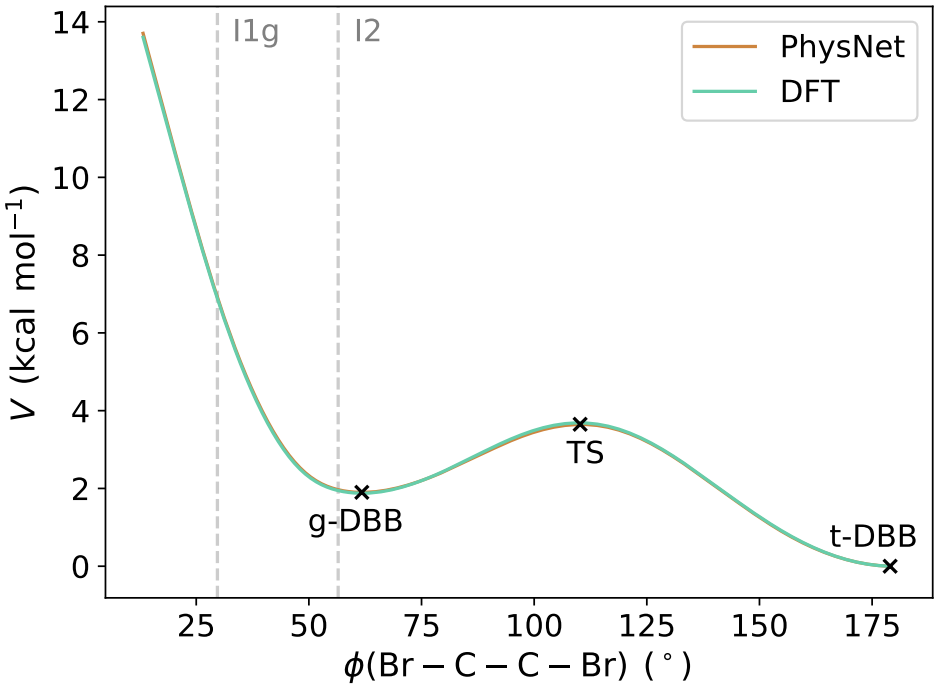

Fig. S11: Relative energies of *gauche-*/*s-trans*-DBB and their isomerization barrier as determined from the PhysNet PES and at the DFT level of theory. The dihedral angles of the two intermediates, $\mathrm{I1}^{\mathrm{g}}$ and I2, of the gauche-DBB reaction paths are illustrated by the vertical dashed lines. Note that, in contrast to the potential energy curve shown here, $\mathrm{I1}^{\mathrm{g}}$ and I2 have formed a complex with Ca^+.

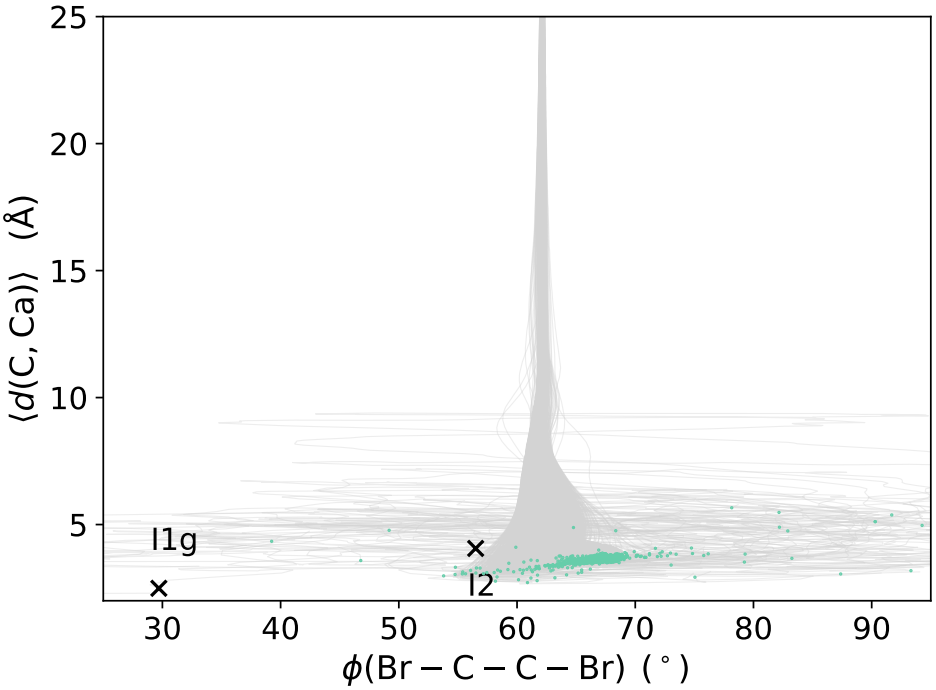

Fig. S12: Evaluation of the reaction pathway for the *gauche*-DBB simulations for impact factor $b = 0$ Å and $j = 0$. The trajectories are shown up to reaction, i.e. up to the point for which a C–Br bond is broken and exceeds 3.0 Å (the equilibrium bond distance is 1.92 Å). The turquoise points mark the snapshot at which (one of the) Br–Ca distances becomes $\leq$ 2.5 Å for the first time (the equilibrium distance of Br–Ca in I3 is $\sim$ 2.5 Å.

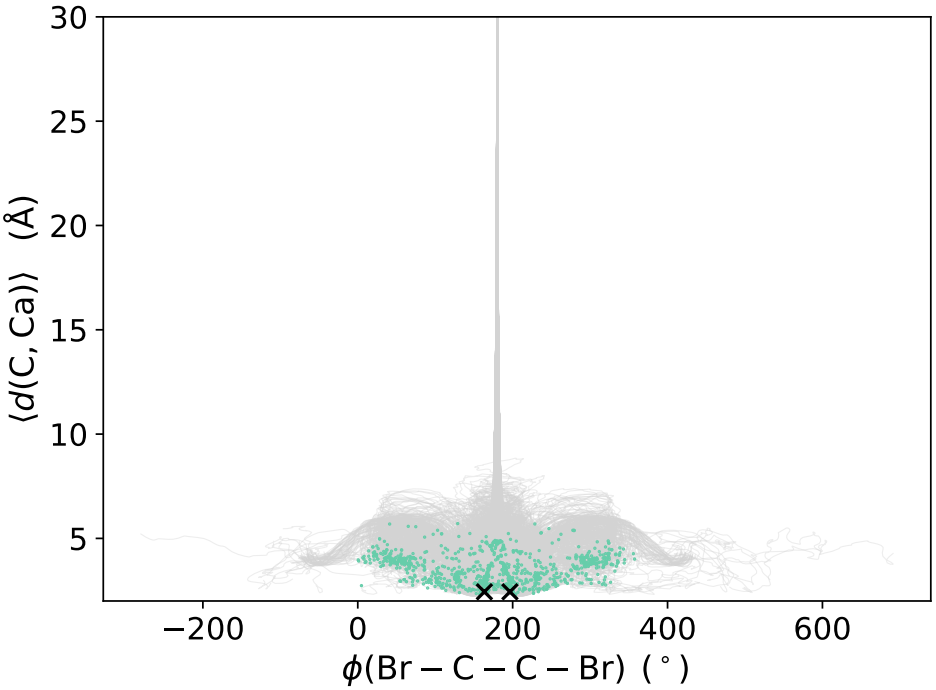

Fig. S13: Evaluation of the reaction pathway for the *s-trans*-DBB simulations for impact factor $b = 0$ Å and $J = 0$. Note that a total of 47 trajectories are excluded from the analysis, because of a longer time to reaction (however, changed the dihedral angle). The trajectories are shown up to reaction, i.e. up to the point for which a C–Br bond is broken and exceeds 3.0 Å (the equilibrium bond distance is 1.93 Å). The turquoise points mark the snapshot at which (one of the) Br–Ca distances becomes $\leq$ 2.5 Å for the first time. The two symmetric pathways via $I1^t$ are visible where $I1^t$ is indicated by black crosses.

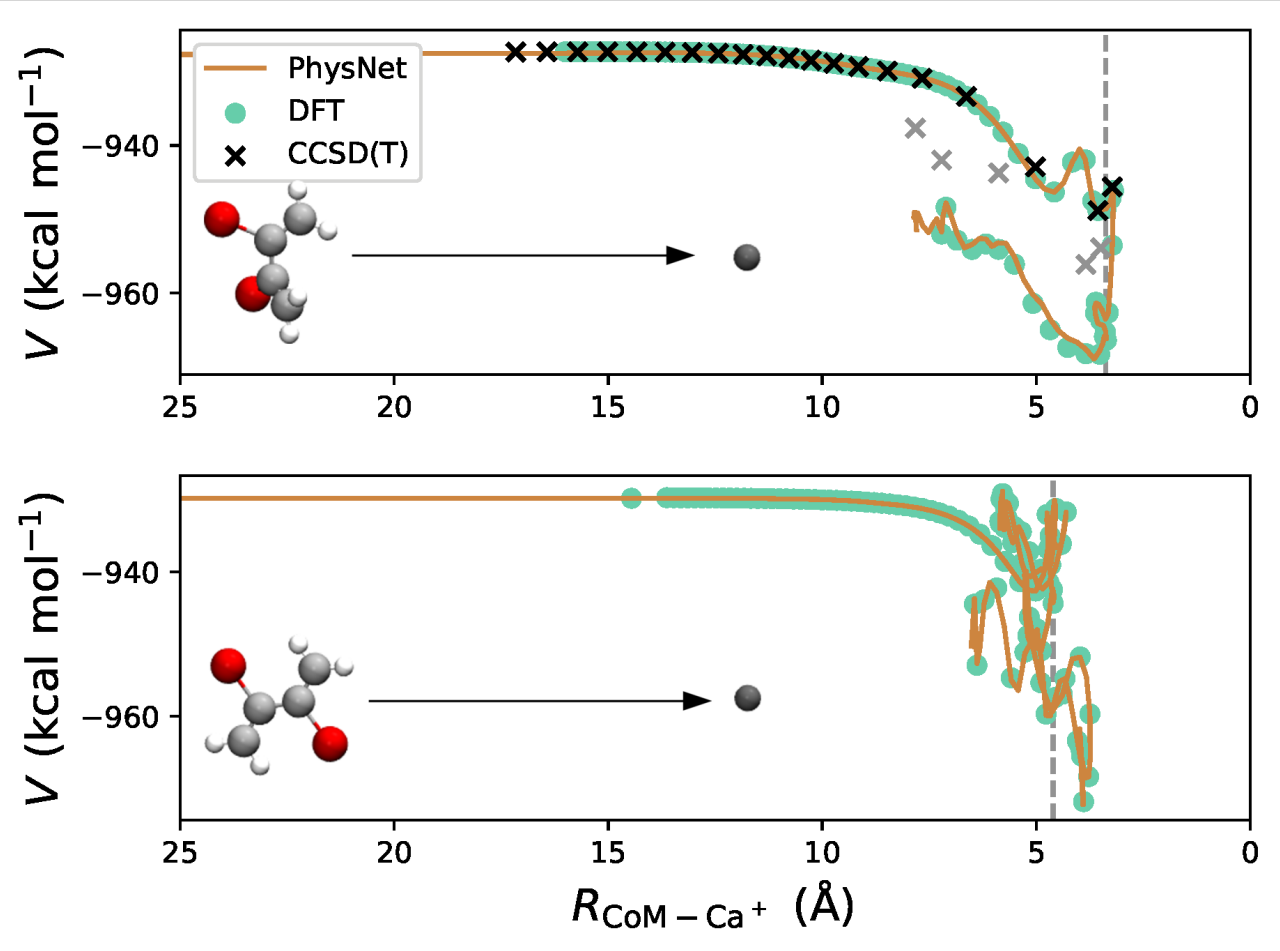

Fig. S14: Comparison of PhysNet and DFT energies for a representative trajectory (impact factor $b = 0$ Å) run for gauche- and trans-DBB using the PhysNet PES. The energies correspond to energies with respect to the free atoms (i.e. total atomization) and corresponds to the quantity PhysNet has been trained on. $R^{+}_{\mathrm{CoM-Ca}}$ is the distance between the CoM of DBB and the Ca^{+} cation. The vertical gray lines mark the reaction point and single CCSD(T)/aVTZ level energies are shown. Note that the CCSD(T) energies have been shifted to match the DFT energy in the entrance channel. Black and gray crosses correspond to snapshots before and after reaction. The T1 diagnostics for the CCSD(T) calculation remains below 0.018 for structures before the reaction and below 0.021 overall.

References

[1] D. Rösch, H. Gao, A. Kilaj and S. Willitsch, *EPJ Tech. Instrum.*, 2016, **3**, 5.

[2] D. A. Dahl, *SIMION 3D, version 6.0 user's manual*, Idaho National Engineering Laboratory, Chemical Materials & Processes Department and Lockheed Idaho Technologies Company, Idaho Falls, Rev. 4 edn, 1995.

[3] D. Clary, *J. Chem. Soc., Faraday Trans. 2*, 1987, **83**, 139–148.

[4] T. Stoecklin, D. C. Clary and A. Palma, *J. Chem. Soc. Faraday Trans.*, 1992, **88**, 901.

[5] Y.-P. Chang, K. Dlugolecki, J. Küpper, D. Rösch, D. Wild and S. Willitsch, *Science*, 2013, **342**, 98–101.

[6] A. Kilaj, H. Gao, D. Rösch, U. Rivero, J. Küpper and S. Willitsch, *Nat. Commun.*, 2018, **9**, 2096.

[7] B. J. Lynch, P. L. Fast, M. Harris and D. G. Truhlar, *J. Phys. Chem. A*, 2000, **104**, 4811.

[8] C. Lee, W. Yang and R. G. Parr, *Phys. Rev. B: Condens. Matter. Phys.*, 1988, **37**, 785.

[9] A. D. Becke, *J. Chem. Phys.*, 1993, **98**, 5648.

[10] F. Weigend and R. Ahlrichs, *Phys. Chem. Chem. Phys.*, 2005, **7**, 3297.

[11] A. Bergner, M. Dolg, W. Küchle, H. Stoll and H. Preuß, *Mol. Phys.*, 1993, **80**, 1431–1441.

[12] F. Neese, F. Wennmohs, U. Becker and C. Riplinger, *J. Chem. Phys.*, 2020, **152**, 224108.